RSC Advances

ROYAL SOCIETY OF CHEMISTRY

www.rsc.org/advances

The formation mechanism of Er^{3+}-doped heterojunction ms/tz-$BiVO_4$ with enhanced photocatalytic performance under visible light

Ruizhi Chen, Ping Wu, Xueming Ma* and Dongmei Jiang

Department of Physics, East China Normal University, Shanghai 200241, People's Republic of China.

Corresponding author: Xueming Ma

Email: xmma@phy.ecnu.edu.cn

Tel: +86-021-54342939

ABSTRACT

$BiVO_4$ products doped with different proportion of erbium were prepared by a hydrothermal reaction with varied reaction time. X-ray diffraction reveals the phase transformation from the tetragonal zircon $BiVO_4$ to the monoclinic scheelite phases with increasing reaction time even without Er^{3+} doping. Scanning electron microscope shows that the morphology of the samples transform from irregular structure to rod-like shape accompanied with the crystalline phase transformation. UV-vis diffuse reflectance spectra and transmission electron microscope indicate that a core-shell structure may form in the meantime. Photocatalytic performance tests have been performed and mechanism of improved photocatalytic performance is discussed. In the end, the formation mechanism of the core-shell structure samples and effect of the Er^{3+} in the crystalline phase transformation are further discussed.

1. Introduction

Semiconductor-based photocatalysis has received much attention over the past decades as a novel environment control technology.[1-3] In order to have a better utilization of solar energy, numerous studies have focused on the development of photocatalysts with high efficiency under visible light irradiation.[4] A great number of novel photocatalysts showing excellent visible absorption ability have been developed, such as Bi_2O_3, Bi_2MoO_6, $InTaO_4$, Bi_2WO_6, $AgNbO_3$, Fe_2O_3, CeO_2, $BaTiO_3$ and $BiVO_4$.[5-15]

$BiVO_4$ has attracted extensive attention for its superior photocatalytic property under visible light irradiation.[16] $BiVO_4$ mainly occurs as a mineral in three crystalline phases: monoclinic scheelite, tetragonal zircon, and tetragonal scheelite.[17, 18] Monoclinic scheelite $BiVO_4$ (ms-$BiVO_4$) shows the best visible-light-driven photocatalytic performance because of its narrow band gap (2.4 eV), while the tetragonal zircon $BiVO_4$ (tz-$BiVO_4$) exhibits very low photocatalytic performance due to the wide band gap (2.9 eV).[19-21] There are still many problems restricting the utilization of the photocatalysts, such as the poor charge-transport characteristics and the weak surface adsorption properties.

For the sake of improving the photocatalytic performance of $BiVO_4$, numerous preparation and modification methods have been developed.[22-24] Lanthanide ions can easily generate multiple electron configurations which exhibit a special optical properties because they have abundant energy levels and 4f electron transitions. Nanoparticles doped with trivalent lanthanide ions can convert low-energy radiation (visible light or NIR) into higher energy radiation (UV-light). This up-conversion property can increase the number of incoming radiation photons for photocatalysis. Lots of researches on

Er^{3+}-doped systems have been reported for the richer spectra of Er^{3+} in the NIR-UV range, which showed the successfully cooperative electronic and luminescence mechanism.[25, 26] With lanthanide doping in the $BiVO_4$, a heterojunction structure is obtained in which the ms-$BiVO_4$ and tz-$BiVO_4$ are coexisting. And the photocatalytic activities of this catalyst have been greatly improved. Recently, Colón et al. reported a $BiVO_4$ heterojunction doped with Er^{3+} by microwave-assisted hydrothermal method which shows great photocatalytic performance because of the combination of heterojunction, Er^{3+} doping and photoluminescence.[27] In their work, the effect of the Er^{3+} doped in the photocatalysis are thoroughly investigated which indicated that the Er^{3+}-doped tz-$BiVO_4$ with photoluminescence will absorb more photons for the ms-$BiVO_4$ part. Besides, classic theory of doping are involved in the process of photocatalysis enhancement. Tan et al. reported that the $BiVO_4$ doped with Nd^{3+}, Sm^{3+}, Yb^{3+} all show a coexistence of ms-$BiVO_4$ and tz-$BiVO_4$. [28-30]

In this work, $BiVO_4$ samples doped with certain proportion of erbium are synthesized by a hydrothermal method with different reaction time. The ms/tz-$BiVO_4$ heterojunction with core-shell structure is proved by the XRD, SEM, TEM, XPS and DRS. And the formation mechanism of the heterojunction is discussed. Photocatalytic activities of these samples reveals a best reaction time for the heterojunction. To further investigate the role of Er^{3+} doped in the transformation process, samples with different proportions of Er^{3+} doping and reaction time are synthesized. XRD of the samples shows that Er^{3+} doping can keep the $BiVO_4$ as tetragonal zircon crystalline phase.

2. Experimental

2.1 Synthesis of photocatalysts

All chemicals used in this work were of analytical reagent grade and obtained from Sinopharm Chemical Reagent Co., Ltd. Er^{3+}-doped $BiVO_4$ photocatalysts were obtained by means of a simple hydrothermal method. Firstly, 5 mmol $Bi(NO_3)_3{\cdot}5H_2O$ was dissolved in 10 mL acetic acid and stirred for 25 min at room temperature to form a white suspension. A corresponding stoichiometric ratio amount of NH_4VO_3 was dissolved in 60 mL hot distilled water and stirred for 25 min at a temperature of 80 ℃. Then the NH_4VO_3 solution was added into the $Bi(NO_3)_3{\cdot}5H_2O$ suspension under vigorous stirring to form a deep orange suspension. After stirring for 5 min, the pH of the obtained suspension was adjusted to 9.0 by adding concentrated NH_4OH (13 $mol{\cdot}L^{-1}$). Afterwards, different amounts of $Er(NO_3)_3{\cdot}6H_2O$ ($n_{Er}:n_{(Er+Bi)}$ = 0, 0.75, 4 at%) were added into these suspensions, respectively. After 30 min of stirring, the mixtures were transferred to 100 mL Teflon-lined stainless autoclaves. The hydrothermal reactions were performed at 140℃ for different periods of time (1 h, 1.5 h, 2 h, 2.5 h, 3 h and 6 h). The obtained precipitates were washed with distilled water and absolute ethanol three times, then dried at 80 ℃ for 12 h. Afterwards, the obtained samples were annealed at 300 ℃ for 2 h. These samples were named as 0.75 at%-0 h-BVO, 0.75 at%-1 h BVO, 0.75 at%-1.5 h BVO, 0.75 at%-2 h BVO, 0.75 at%-2.5 h BVO, 0.75 at%-3 h BVO, 0.75 at%-6 h BVO, 0 at%-1.5 h BVO, 0 at%-2.5 h BVO, 4 at%-1.5 h BVO, 4 at%-2.5 h BVO, respectively. And the bare $BiVO_4$ was synthesized by the same method.

2.2 Characterization of photocatalysts

The crystalline phases of as synthesized samples were identified by X-ray powder diffraction (XRD) using a Bruker AXS/D8 ADVANCE with Cu/Kα (λ =1.540568 Å) radiation at 40 kV and 40 mA. Rietveld analysis was performed by the Maud program over the selected samples. Field emission scanning electron microscopy (FESEM) images were performed on a SERION field emission scanning electronic microscope equipped with an energy-dispersive X-ray (EDX). X-ray photoelectron spectroscopy (XPS) measurements were carried out on a RBD upgraded PHI-5000C ESCA system (Perkin Elmer) with an Mg/Kα source (*hv*=1253.6 eV). Inductively coupled plasma (ICP) measurements were carried out using a sequential viewed in ductively coupled plasma emission spectrometer (PE Optima 7000, USA). UV-Vis diffuse reflectance spectra (DRS) was recorded with a Shimadzu UV2550 recording spectrophotometer. Raman measurements were performed using a Laser Confocal Micro-Raman Spectroscopy (LabRAM HR800, Horiba Jobin Yvon Company). Laser radiation (λ=532 nm) was used as excitation source at 5 mW. Transmission electron microscopy (TEM) images were collected using a JEOL model JEM 2010 EX electron microscope at an accelerating voltage of 200 kV.

2.3 Evaluation of photocatalytic activity

Photocatalytic activities of the as-prepared samples were evaluated by degradation of methylene blue under visible light irradiation. The experiments were performed at room temperature as follows: 0.05 g photocatalyst was dispersed into 50 mL methylene blue solution (10 mg/L, neutral condition) and stirred magnetically for 30 min in dark to establish an adsorption-desorption equilibrium. Then the suspension was illuminated in a photoreaction apparatus with a 500 W Xe lamp (GXZ500, Shanghai Jiguang Special

Lighting Electrical Appliance). At an intervals of 15 min, about 2 mL of suspension was taken out, centrifuged and analysed by a UV-Vis spectrometer (Perkin-Elmer Lambda 750S) with deionized water as reference sample.

3. Results and discussion

3.1 Crystal structure analysis (XRD)

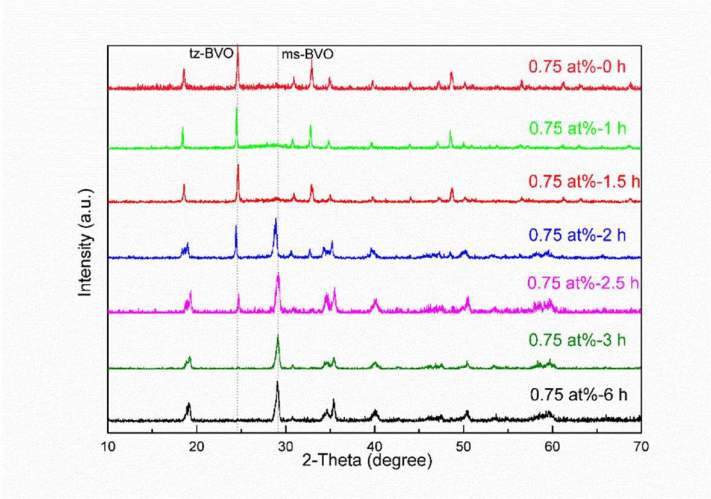

Fig.1 X-ray diffraction patterns of the 0.75% Er^{3+}-doped $BiVO_4$ samples with different reaction time.

Fig. 1 shows XRD patterns of 0.75 at% Er^{3+}-doped $BiVO_4$ with different reaction time. All diffraction peaks of Er^{3+}-doped $BiVO_4$ without hydrothermal treatment are in agreement with the standard card of tz-$BiVO_4$ (PDF 14-0133). No obvious ms-$BiVO_4$ diffraction peaks can be observed in sample with 1 h hydrothermal treatment. With the increase of time of hydrothermal reaction, it can be clearly observed that the monoclinic scheelite phase (PDF 75-1866) appears and no signal of other phases about Er^{3+} or impurities can be detected. A double crystalline phase coexistence can be clearly observed with a reaction time of 2 h or 2.5 h. When the reaction time reach to 3 h, only a very small diffraction peaks of tz-$BiVO_4$ can be observed. Calculated from Rietveld analysis (Table 1), the

tetragonal zircon phase gradually decrease while the monoclinic scheelite phase increasing in the meantime. Eventually, after 6 h of reaction, the Er^{3+}-doped $BiVO_4$ completely transformed to ms-$BiVO_4$. A clear tendency of the crystalline phase transformation from tz-$BiVO_4$ to ms-$BiVO_4$ can be observed, which is in agreement with the previously report about the $BiVO_4$ crystal transformation.[18, 27]

Table 1. Structure features from Rietveld analysis for Er^{3+} doped $BiVO_4$ catalysts

samples	monoclinic schelite			tetragonal zircon		tetragonal zircon
	a	b	c	a=b	c	(wt%)
0.75 at%-1 h BVO				7.3004	6.4576	90.9
0.75 at%-1.5 h BVO	5.1909	5.1065	11.6934	7.2978	6.4552	83.8
0.75 at%-2 h BVO	5.2022	5.1058	11.7104	7.2965	6.4559	28.7
0.75 at%-2.5 h BVO	5.2027	5.1071	11.7063			15.3
0.75 at%-3 h BVO	5.2013	5.0992	11.7019			3.3
0 at%-1.5 h BVO	5.2024	5.1004	11.7011	7.2963	6.4547	21.7
0 at%-2.5 h BVO	5.1999	5.1065	11.7020			1.2
4 at%-1.5 h BVO				7.3002	6.4565	96.4
4 at%-2.5 h BVO	5.2134	5.1061	11.7070	7.2982	6.4555	61.1

To further study the role of Er^{3+} doped in the transformation, $BiVO_4$ samples with different proportions of Er^{3+} doping and reaction time were synthesized. Fig. S1 shows XRD patterns of three other groups for contrast (0 at% Er^{3+}-doped, 0.75 at% Er^{3+}-doped, 4 at% Er^{3+}-doped with the reaction time of 1.5 h and 2.5h, respectively). The samples without doping show a quick transformation from the tz-$BiVO_4$ to ms-$BiVO_4$. With the Er^{3+} doped increasing to 0.75 percentage, the transformation becomes slower than the non-doping samples. Samples with 4 at% Er^{3+} doped show the slowest transformation. This result shows that even without Er^{3+} doping, a heterojunction can appear, which indicates that Er^{3+} doping is not the reason for the heterojunction. Compared with the other two groups, a fact can be derived that with the increase of Er^{3+}, the transformation from tz-$BiVO_4$ to ms-$BiVO_4$ is hindered. These facts show that Er^{3+} doping is a key factor to

maintain the stability of the tz-$BiVO_4$, but not the origin of the heterojunction. These inferences do not agree with the conclusion of previous reports, which believed the origin of the heterojunction were the lanthanide ions doping.[27] We inferred that the tz-$BiVO_4$ forms at the very beginning when the $Bi(NO_3)_3$ and NH_4VO_3 were mixed, after which the tz-$BiVO_4$ transformed to ms-$BiVO_4$ until a complete transformation.

3.2 Elemental analysis (XPS and ICP)

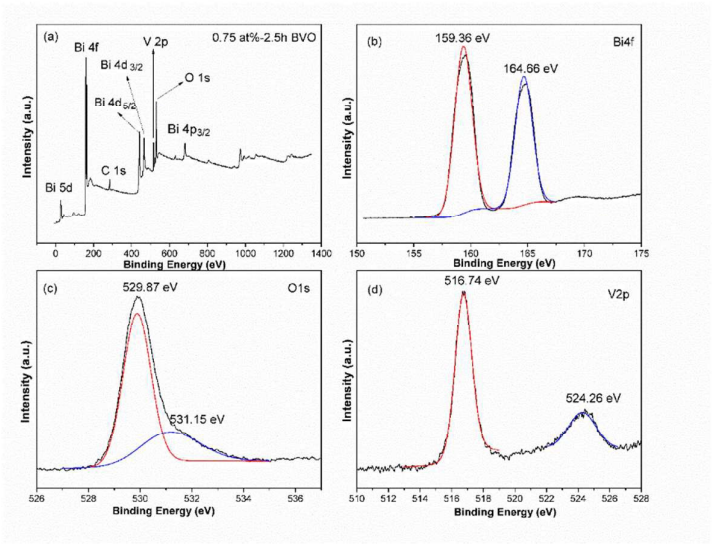

Fig. 2 XPS spectra of 0.75 at%-2.5 h $BiVO_4$ samples: (a) survey scan, (b) Bi4f, (c) O1s and (d) V2p.

Fig. 2 shows the XPS spectra of 0.75 at%-2.5 h $BiVO_4$. The relevant peak position is calibrated against the C1s signal of contaminant carbon at a binding energy of 284.6 eV. Fig. 2(a) is a typical survey spectrum, and only Bi, V, O and trace amount of C are detected. No obvious peaks related to Er are observed. This is because of the low concentration of Er^{3+} doping. Fig. 2(b)-(d) are the high-resolution spectra of Bi4f, V2p and O1s. The strong peaks at 164.66 eV and 159.36 eV (Fig. 2(b)) corresponding to $Bi4f_{5/2}$ and $Bi4f_{7/2}$ are characteristics of Bi^{3+}, indicating that the Bi species in the composite exist as Bi^{3+}. The peaks located at 529.87 eV (Fig. 2(c)) can be assigned to the oxygen species of

lattice oxygen of layer-structured $Bi_2O_2^{2+}$. The O1s peak at binding energy of 531.15 eV may come from adsorbed H_2O or surface hydroxyl group. The V2p peaks can be fitted with two peaks at 524.26 eV and 516.74 eV, which are assignable to $V2p_{1/2}$ and $V2p_{3/2}$ signals, respectively (Fig. 2(d)). Based on the XRD and XPS results, it is reasonable to deduce that the as-prepared composites are $BiVO_4$.

To confirm the existence of Er^{3+}, the inductively coupled plasma measurements are performed as shown in Table 2. The actual proportion is lower than that of the design. This may due to the loss during the preparation process.

Table 2. The inductively coupled plasma results of samples with different dopant

sample	Er (wt%)	Er (at%)	Bi (wt%)	V (wt%)
0.75 at%-2.5 h-BVO	0.15	0.29	72.11	14.57
4 at%-2.5 h-BVO	1.39	2.69	73.58	14.88

3.3 Morphology analysis (FE-SEM and EDX)

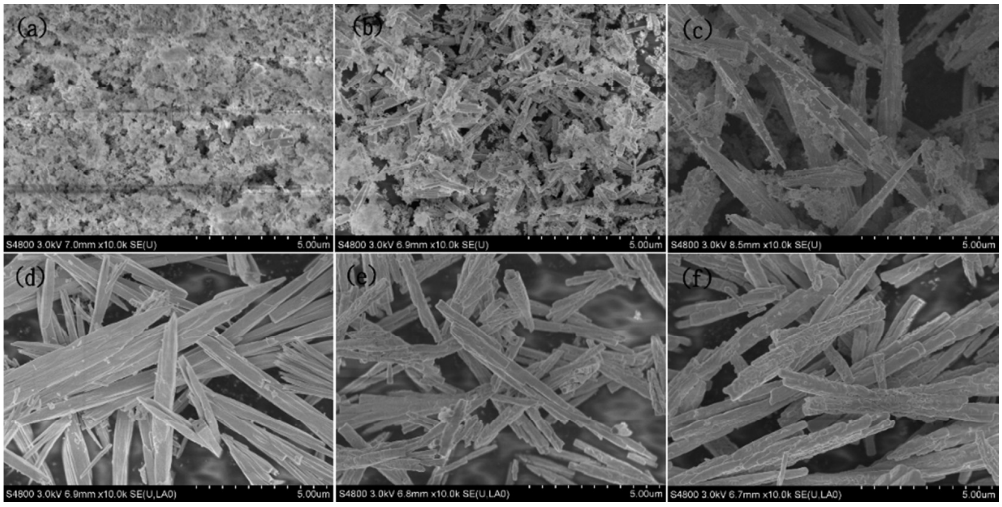

Fig.3 FE-SEM images of the samples with heating (a) 1 h, (b) 1.5 h, (c) 2 h, (d) 2.5 h, (e) 3 h and (f) 6 h.

FE-SEM images of samples with different reaction time are shown in Fig. 3. A morphology evolution of the samples can be clearly observed. The sample with 1 h reaction time (Fig. 3(a)) is formed by a few rods mixed with lots of irregularly shaped objects. With the increasing of reaction time, the rod-shaped objects get more and bigger until almost all the irregularly shaped objects turn into the regular rod-shaped structure when the reaction time reaches 2.5 h (Fig. 3(d)). The length of rod-like samples is about 10-15 μm and the width of which is about 400-600 nm. The rod-shaped structure starts to break down with the increase of reaction time which leads to the shrinking and the surface-roughening of samples (Fig. 3(e), (f)). Combined with the XRD results of samples, we can infer that the irregularly shaped objects are the tz-$BiVO_4$ which is in an initial state. And the transformation from the irregular shape to the rod-like shape happens simultaneously with the transformation from the tz-$BiVO_4$ to the ms-$BiVO_4$. The rod-shaped part contains two type of $BiVO_4$ which is a relatively stable state. If the reaction time exceeds 2.5 h, tz-$BiVO_4$ phase in these rods starts to change into ms-$BiVO_4$ phase and leads to the shrinkage and surface-roughening of the rods.

3.4 Spectral analysis (DRS and Raman spectra)

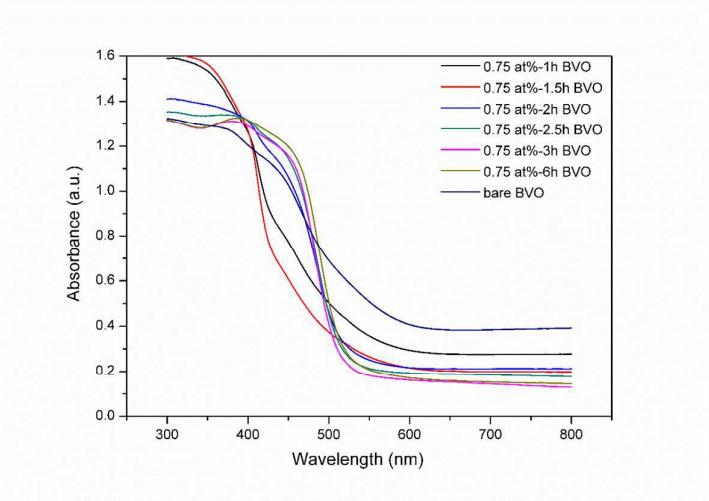

Fig. 4 UV-vis absorption property of 0.75 at%-$BiVO_4$ with different reaction time.

The phase transformation mentioned above also has a significant impact on the optical absorption properties of the samples. Fig. 4 shows the UV-vis diffuse reflectance spectra of the Er^{3+}-doped $BiVO_4$ with different reaction time. From the DRS, two clear absorption edges can be noticed with the transformation from the tz-$BiVO_4$ to ms-$BiVO_4$. However, no obvious coexistence absorption edges of the two crystal phase can be noticed especially in the 0.75 at%-2 h BVO and the 0.75 at%-2.5 h BVO samples, which have a difference with the previous reports.[27, 31] The absorption edge is mainly due to the ms-$BiVO_4$ crystal phase and only a very small absorption edge of the tz-$BiVO_4$ can be noticed in the spectra. This might be because the tz-$BiVO_4$ crystalline phase is existing inside the samples. The tz-$BiVO_4$ crystalline phase in the surface turns into the ms-$BiVO_4$ more easily and the transformation occurs from the surface to the inside with the increase of reaction time. Considering the thickness of ms-$BiVO_4$ in the surface of the rods, it may be difficult for light to penetrate the surface to obtain optical absorption properties of the core, which leads to disappearance of the absorption edge of the second crystal phase. The absorption in the UV area of tz-$BiVO_4$ is higher than samples

containing more ms-$BiVO_4$ with reaction time increasing. Band gap energy (*Eg*) values are calculated from the UV-vis DRS using the equation $Eg=1240/\lambda$, where λ is the wavelength of the absorption onset.[32, 33] The calculated band gap values at 2.38 eV and 2.76 eV from these two absorption edges would be associated to the monoclinic scheelite and tetragonal zircon phases respectively, which are a little bit lower than that of pure $BiVO_4$ reported in the literature because of the Er^{3+} doping. Previous literature discovered two minor bands at 525 nm and 655 nm, which could be associated to the presence of Er^{3+} and could be assigned to the transition from the $4I_{15/2}$ ground state to the $4H_{11/2}$ and $4F_{9/2}$ excited states.[27] No minor bands can be found at 525 nm and 655 nm in our sample, which is due to the low concentration of Er^{3+} doping.

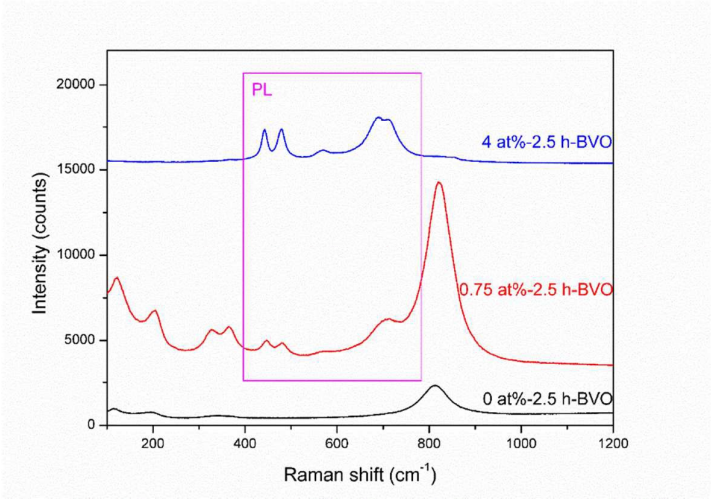

Fig. 5 Raman spectra of samples with different Er^{3+} doping upon 532 nm laser excitation.

Fig. 5 shows the Raman spectra of samples with different Er^{3+} doping upon 532 nm laser excitation. Raman bands around 158, 208, 324, 362 and 826 cm^{-1} are observed, which are typical vibrational bands of ms-$BiVO_4$. The luminescence bands corresponding to the fluorescence emission of Er^{3+} can be detected as erbium is present. With the Er^{3+}

increasing, the luminescence properties become stronger. The results show that luminescence process occurs even with a low dopant of 0.75 at% Er^{3+}.

3.5 Transmission electron microscope analysis (TEM and HR-TEM)

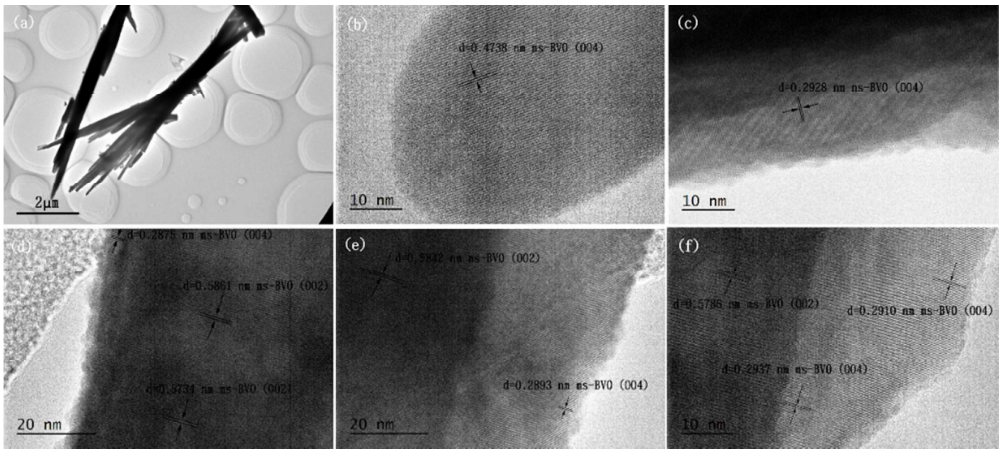

Fig. 6 TEM and HR-TEM images of the 0.75 at%-2.5 h BVO samples.

To verify the core-shell structure inferred from the DRS spectra, TEM and HR-TEM images of the 0.75%-2.5 h BVO sample are shown in Fig. 6. Fig. 6(a) shows the overall appearance of samples, one of which appears as a combination of multiple rod-shaped objects. Fig. 6(b)-(e) show the HR-TEM of the surface part of the rod-shaped samples. In all HR-TEM images, none tz-$BiVO_4$ can be observed which shows that the tz-$BiVO_4$ probably exists inside the samples. Combined with the DRS and XRD spectra, we can prove that the rod-shaped $BiVO_4$ simples are core-shell structure. However, this $BiVO_4$ is not a typical core-shell structure, because the phase transformation occurs from the early period of reaction, which means the tz-$BiVO_4$ and ms-$BiVO_4$ will coexist in the core of the rod samples.

3.6 Photocatalytic activity

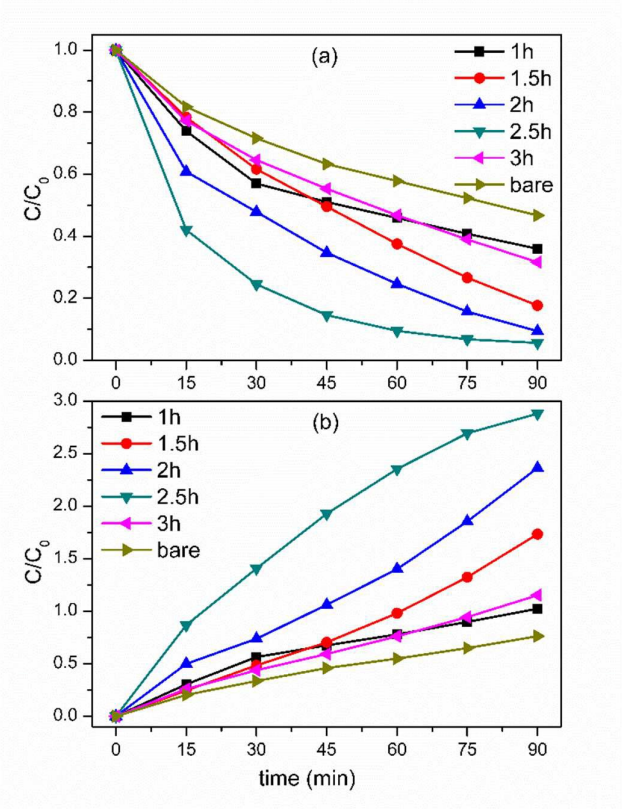

Fig. 7 The photodegradation of methylene blue under visible light irradiation for 0.75 at% $BiVO_4$ with 1 h, 1.5 h, 2 h, 2.5 h, 3 h and bare $BiVO_4$.

Photocatalytic degradation of aqueous phase of methylene blue was performed to evaluate the photocatalytic activity of photocatalysts. Fig. 7 shows the concentration changes of methylene blue versus visible-light irradiation time in the photocatalytic process. It is worthy to note that $BiVO_4$ samples with same Er^{3+} doping show different photocatalytic activity. With reaction time increasing from 1 h to 2.5 h, the photocatalytic activity peaks. But with reaction time further increasing, the photocatalytic activity become worse. The best photocatalytic performance was achieved by 0.75 at. % Er^{3+} doped $BiVO_4$ with 2.5 h reaction time.

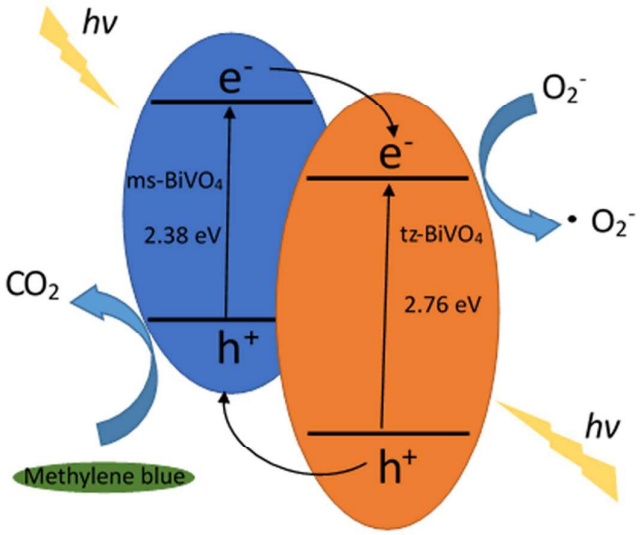

Fig. 8 Schematic diagram of charge separation in a visible-light irradiated heterojunction.

Fig. 8 shows the schematic diagram illustrating their photoexcited carrier migration and reactions in the heterojunction. Under visible-light irradiation, both ms-$BiVO_4$ and tz-$BiVO_4$ can be excited to generate electron-hole pairs. The photogenerated free electrons could either be recombined with the free holes or could be transferred from the conduction band of ms-$BiVO_4$ into the conduction band of tz-$BiVO_4$, while the excited holes on the valence band of tz-$BiVO_4$ can be transferred to the valence band of ms-$BiVO_4$. Thus, the separation of photogenerated carriers will be promoted by the band energy differences that appear after the heterojunction formation. When the ms-BiVO4 and tz-$BiVO_4$ are in contact under irradiation, the electron and hole transfer between the semiconductors makes the Fermi level of ms-$BiVO_4$ to move down, while that of tz-$BiVO_4$ moves up until a pseudo-equilibrium is reached. The separation of photogenerated electron-hole pairs in two different phases prevent charge recombination. Charges will be free to initiate reactions with the reactants adsorbed on the photocatalyst surface, and thereby promote and enhance the photocatalytic activity of the samples. The best

performance of the samples could dues to the optimization of heterojunction and favourable morphology.

The role of Er^{3+} doped in the luminescence properties of Er^{3+}-doped $BiVO_4$ photocatalysts has already been investigated in detail. Colón et al. claimed that only when Er^{3+} occupies the Bi^{3+} sites in the tz-$BiVO_4$ structure, visible luminescence can be noticed. And it would be expected that ms-$BiVO_4$ would have certain extra photons available from luminescence process.[27] Considering the above structural and luminescence properties, the complex cooperative mechanism involved in the overall process can be envisaged. When Er^{3+} is doping the monoclinic phase, dopant would help to the charge separation till its concentration is detrimental and promote the recombination process.[34] On the other hand Er^{3+} doped in the tz-$BiVO_4$ can produce visible luminescence, which provides more photons into the photocatalysis process. And the heterojunction formed by the ms-$BiVO_4$ and tz-$BiVO_4$ can promote the separation of photoinduced electron-hole pairs.

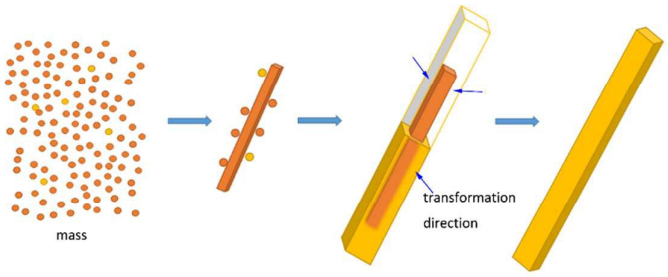

Fig. 9 The illustration of the formation mechanism for samples as reaction time increasing.

Our work concentrates on the formation mechanism of core-shell structure and the effect of Er^{3+} doping on the mechanism of heterojunction. By modifying synthetic reaction time, Er^{3+} doped $BiVO_4$ with different structural and optical behavior and a dramatic

enhanced photoactivity are obtained. The structure features and their phase evolutions with increasing reaction time show a great difference with the previous report, which confirm the role of the precursor addition sequence.[27] The transformation from tz-$BiVO_4$ to ms-$BiVO_4$ can be noticed by the XRD results. From the DRS and HR-TEM results, we can confirm a core-shell structure with the ms-$BiVO_4$ as the shell and the commixture of the ms-$BiVO_4$ and tz-$BiVO_4$ as the core. We have a very clear conclusion about the formation mechanism of the Er^{3+} doped $BiVO_4$. Fig. 9 shows the illustration of the formation mechanism for samples as reaction time increasing. When vanadate is added to Bi^{3+} solution, the precipitation of $BiVO_4$ has been present with the tetragonal zircon crystalline phase with or without the addition of Er^{3+}. Previous works have mentioned tetragonal zircon $ErVO_4$ may occur when mixing the NH_4VO_3 and $Er(NO_3)_3$.[27] It could be assumed that $ErVO_4$ small seeds form in the tetragonal phase after Er^{3+} added to the mixture. And the tetragonal zircon $ErVO_4$ will prevent the transformation from ms-$BiVO_4$ to tz-$BiVO_4$. The transformation slowing down with the Er^{3+} doping increase can be well explained. The phase transformation from tz-$BiVO_4$ to ms-$BiVO_4$ occurs in the hydrothermal reaction process. During this process, the morphology changes to rod-like shape from irregular shape. And the transformation occurs from the surface of the sample to the core, so a core-shell structure can be formed. This transformation can produce a tighter heterojunction which can promote the separation of photoinduced electron-hole pairs thus improve the photocatalytic activity.

Conclusions

In conclusion, $BiVO_4$ products doped with different proportion of erbium by a hydrothermal method with different hydrothermal reaction time were successfully synthesized. By controlling the reaction time of hydrothermal reaction, a series of products were synthesized in which a phase transformation from tz-$BiVO_4$ to ms-$BiVO_4$ was observed. By comparing the effect of different percentage of the Er^{3+} doping, a mechanism that Er^{3+} doping is the reason for maintain the $BiVO_4$ as the tetragonal zircon crystalline phase can be verified. DRS and TEM show the samples are a kind of core-shell structure, which also confirms the phase transformation. The photocatalytic experiment shows the photocatalytic performance greatly depends on crystalline phase and morphology, and the 0.75 at%-2.5 h BVO sample exhibits the best performance. The enhancement of photocatalytic performance comes from three main factors: the strong luminescence behavior from Er^{3+} doped in the tz-$BiVO_4$, the help of the charge separation by Er^{3+} doped in the ms-$BiVO_4$ and the heterojunction which promotes the separation of photoinduced electron-hole pairs. As far as we know, this is the first time to investigate the formation mechanism of Er^{3+} doped heterojunction ms/tz-$BiVO_4$. This mechanism may be extended to the whole lanthanide ions doped in $BiVO_4$.

References

1. W. Zhao, Y. Liu, Z. Wei, S. Yang, H. He and C. Sun, *Appl Catal B-environ*, 2016, **185**, 242-252.
2. J. Xia, J. Di, H. Li, H. Xu, H. Li and S. Guo, *Appl Catal B-environ*, 2016, **181**, 260-269.
3. J. Xiao, Y. Xie, H. Cao, F. Nawaz, S. Zhang and Y. Wang, *J Photoch Photobio A*, 2016, **315**, 59-66.
4. S. Tripathi, S. N. Singh and L. D. S. Yadav, *RSC Adv.*, 2016, **6**, 14547-14551.
5. W. Gou, P. Wu, D. Jiang and X. Ma, *J Alloy Compd*, 2015, **646**, 437-445.
6. A. Phuruangrat, S. Putdum, P. Dumrongrojthanath, N. Ekthammathat, S. Thongtem and T. Thongtem, *Mater Sci Semicon Process*, 2015, **34**, 175-181.

7. Y.-C. Chiou, U. Kumar and J. C. S. Wu, *Appl Catal A-Gen*, 2009, **357**, 73-78.
8. J. Li, Z. Liu and Z. Zhu, *Appl Surf Sci*, 2014, **320**, 146-153.
9. W. Wu, S. Liang, Y. Chen, L. Shen, R. Yuan and L. Wu, *Mater Res Bull*, 2013, **48**, 1618-1626.
10. T.-W. Sun, Y.-J. Zhu, C. Qi, G.-J. Ding, F. Chen and J. Wu, *J Colloid Interface Sci*, 2016, **463**, 107-117.
11. Z.-R. Tang, Y. Zhang and Y.-J. Xu, *RSC Advances*, 2011, **1**, 1772.
12. Y. Ni, H. Zheng, N. Xiang, K. Yuan and J. Hong, *RSC Adv.*, 2015, **5**, 7245-7252.
13. X. Dang, X. Zhang, X. Dong, W. Ruan, H. Ma and M. Xue, *RSC Adv.*, 2014, **4**, 54655-54661.
14. B. Yuan, R. Chong, B. Zhang, J. Li, Y. Liu and C. Li, *Chem Commun*, 2014, **50**, 15593-15596.
15. Y. Zhang, Y. Guo, H. Duan, H. Li, C. Sun and H. Liu, *Phys Chem Chem Phys*, 2014, **16**, 24519-24526.
16. Y. Park, K. J. McDonald and K.-S. Choi, *Chem Soc Rev*, 2013, **42**, 2321-2337.
17. R. L. Frost, D. A. Henry, M. L. Weier and W. Martens, *J Raman Spectrosc*, 2006, **37**, 722-732.
18. G. P. Nagabhushana, A. H. Tavakoli and A. Navrotsky, *J Solid State Chem*, 2015, **225**, 187-192.
19. Y. Guo, X. Yang, F. Ma, K. Li, L. Xu, X. Yuan and Y. Guo, *Appl Surf Sci*, 2010, **256**, 2215-2222.
20. B. Zhou, X. Zhao, H. Liu, J. Qu and C. P. Huang, *Appl Catal B-environ*, 2010, **99**, 214-221.
21. A. Zhang and J. Zhang, *Spectrochim Acta A Mol Biomol Spectrosc*, 2009, **73**, 336-341.
22. Y. Zhong, J. Wang, R. Zhang, W. Wei, H. Wang, X. Lu, F. Bai, H. Wu, R. Haddad and H. Fan, *Nano Lett*, 2014, **14**, 7175-7179.
23. J. A. Seabold and K. S. Choi, *J Am Chem Soc*, 2012, **134**, 2186-2192.
24. P. M. Rao, L. Cai, C. Liu, I. S. Cho, C. H. Lee, J. M. Weisse, P. Yang and X. Zheng, *Nano Lett*, 2014, **14**, 1099-1105.
25. J. Méndez-Ramos, P. Acosta-Mora, J. C. Ruiz-Morales, M. Sierra, A. Redondas, E. Ruggiero, L. Salassa, M. E. Borges and P. Esparza, *Opt Mater*, 2015, **41**, 98-103.
26. Y. Zhang, R. Selvaraj, M. Sillanpää, Y. Kim and C.-W. Tai, *J Ind Eng Chem*, 2015, **24**, 161-165.
27. S. Obregón and G. Colón, *Appl Catal B-environ*, 2014, **158-159**, 242-249.
28. Y. Luo, G. Tan, G. Dong, H. Ren and A. Xia, *Ceram Int*, 2015, **41**, 3259-3268.
29. Y. Luo, G. Tan, G. Dong, L. Zhang, J. Huang, W. Yang, C. Zhao and H. Ren, *Appl Surf Sci*, 2015, **324**, 505-511.
30. J. Huang, G. Tan, L. Zhang, H. Ren, A. Xia and C. Zhao, *Mater Lett*, 2014, **133**, 20-23.
31. S. Usai, S. Obregón, A. I. Becerro and G. Colón, *The Journal of Physical Chemistry C*, 2013, **117**, 24479-24484.
32. M. Wang, H. Zheng, Q. Liu, C. Niu, Y. Che and M. Dang, *Spectrochim Acta A Mol Biomol Spectrosc*, 2013, **114**, 74-79.
33. Z. He, Y. Shi, C. Gao, L. Wen, J. Chen and S. Song, *The Journal of Physical Chemistry C*, 2014, **118**, 389-398.
34. A. Kubacka, G. Colón and M. Fernández-García, *Catal Today*, 2009, **143**, 286-292.

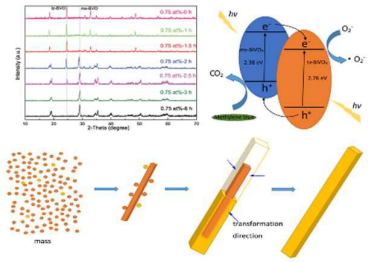

The formation mechanism of Er^{3+} doped heterojunction $BiVO_4$ and enhanced photocatalysis.